

Final Report, Project #20040

PI Clifford Thurber
University of Wisconsin-Madison
March 12, 2021

Research accomplished

Our current SCEC project, award #20040, involves application of joint body wave-surface wave tomography to southern California using the joint inversion code of Fang et al. (2016) with a greatly expanded dataset compared to previous studies. We use multiple starting models, followed by evaluation of the tomographically updated models via wavefield simulation. Specifically, the inversion results and the starting and final models are evaluated for their relative ability to fit waveforms for selected regional earthquakes, using simulations done with SPECFEM3D. The overall goal of our work is to assess whether the combination of (1) assembling an enlarged dataset, taking particular advantage of data from the Salton Sea Imaging Project (SSIP; Han et al., 2016), and (2) applying a joint body wave-surface wave inversion code can (3) produce a seismic velocity model that better fits regional waveforms than the starting models for a set of moderate-sized earthquakes.

The expanded dataset for tomography is shown in Figure 1. It is a combination of (1) earthquake body-wave data selected from the datasets of Fang et al. (2016) and Share et al. (2019), with some additional earthquake body-wave data southwest of the Salton Sea, (2) surface-wave data from Fang et al. (2016), (3) explosion data from Lin et al. (2010), and (4) active-source data from SSIP provided to us by Patricia Persaud of LSU.

We used a procedure we term the best cell event (BCE) method (Guo and Thurber, 2021) to select the earthquakes to include in the inversion. We first meshed the whole study volume uniformly with grid intervals of 3 km in the horizontal directions and 1 km in depth. In each cell, we identified up to three events with the most arrivals and selected the one with highest data quality, which is defined as the BCE. This step is beneficial because it makes the data distribution more uniform spatially and it reduces computation time compared to using all available events. We also constructed differential times for all pairs of the best cell events with inter-events separations less than 6 km. This yields differential times that have more uniform velocity model sensitivities for the regions with concentrated events than the differential data constructed through a standard way using Waldhauser's (Waldhauser, 2001) ph2dt algorithm (Guo and Thurber, 2021). We selected 8,418 earthquakes, which yielded 327,107 absolute P-wave arrival times, 302,095 absolute S-wave arrival times, 2,167,800 P-wave differential times, and 1,747,931 S-wave differential times.

As in Fang et al. (2016), the Rayleigh wave dataset we used is from Zigone et al. (2015) and includes 30,377 group travel times with periods from 3 to 12 s, which were extracted from ambient noise cross-correlation analysis. One potential avenue for future improvement is to add surface-wave data that covers the model region more densely.

The active-source P-wave dataset from Lin et al. (2010) that falls within our study area consists of 10 quarry blasts (unknown origin time) recorded by 141 stations and 47 shots recorded by 1,312 stations. The active-source P-wave data from SSIP includes 2,330 air-gun shots, 126 land shots (explosions), 78 OBS stations in the Salton Sea, and 4,341 land stations around the Salton Sea.

The models are defined on a geographic mesh with 0.06° node spacing in both latitude and longitude and nodes in depth at -1.5, 0, 2, 4, 6, 8, 10, 13, 16, 20, and 26 km. Stations and sources are all positioned at their true elevation. We tested three starting models, the Fang et al. (2016) model, CVM-S4.26, and CVM-H15.10. We performed numerous inversions using different smoothing and damping values to find the optimal values by considering the balance between model roughness and data residual reduction. The damping values for different iterations are also adjusted slightly based on the condition number of the inversion system, which indicates the stability of the inversion.

Due to the fact that the augmented dataset contains much of the original Fang et al. (2016) dataset, the joint inversion starting with that model performed extremely well, reducing the misfit from 0.45 s to 0.10

s for body waves and from 1.44 s to 1.37 s for surface waves. The small improvement in fit for the surface-wave data is because the data and starting model are from Fang et al. (2016), so it is difficult to improve the fit further. In contrast, the body-wave data has been enlarged substantially. An example depth slice through the new model is shown in Figure 2 in comparison to the starting model. The largest changes are in the shallow structure. The result from the CVM-S starting model fits the data much more poorly: 0.17 s for body waves and 17.28 s for surface waves), and the model has unrealistic anomaly amplitudes in the shallow crust. We attribute the poor performance using CVM-S as the starting model to inadequacy of the travel-time calculator. The joint inversion starting from CVM-H did not reach completion, becoming stuck during the travel-time calculations.

The problems with the travel-time calculator are due to the fact that the code uses the spherical-Earth extension (Koketsu and Sekine, 1998) of the pseudo-bending ray tracer (Um and Thurber, 1987). This ray tracer was not designed to handle factors of two or more changes in seismic velocity over distances of a few kilometers (Figure 3). Fortunately, since the Fang et al. (2016) joint inversion code was developed based on the spherical-Earth version of the tomoDD series of body-wave-only tomography codes, this problem can be rectified in the future by replacing the spherical-Earth ray tracer with a finite difference ray tracer used in other versions of tomoDD codes (Zhang et al., 2004; Lin et al., 2010) that can handle models with large, sharp velocity changes.

Using a pre-existing framework for CVM-H forward synthetic model runs using SPECFEM3D (see Toward Full Waveform Tomography Across California (Year 2), Final Report, Project #19017), we were able to create synthetic waveforms for models based on the Fang et al. (2016) results and the updated results presented here (hereafter referred to as the Guo model). To create a velocity model for SPECFEM3D, we embedded the smaller models of Fang et al. (2016) and Guo within the broader CVM-H model. This embedding procedure involved adopting the velocities from Fang et al./Guo in regions characterized by high derivative-weight-sum. In areas of poor coverage in the Fang et al. (2016)/Guo model, the 3D CVM-H velocity anomalies are preserved. An example of the embedding procedure for the Guo model is shown in Figure 4. The 3D CVM-H structure was not used as the starting model for the Fang et al./Guo models and hence these features were not present in the final models due to poor coverage in these regions.

We qualitatively compared observed seismograms with synthetic seismograms from a single event for: a) the CVM-H model, b) the initial Fang et al. (2016) model, and c) the updated Guo model (Figure 5, event epicenter shown in Figure 4). For the filtered period range of 3-20 s, the first arriving wavelet is reasonably well fit by all synthetic waveform models, a fit which degrades over time (10's of seconds). It is also apparent that the 3 models (embedded Guo, embedded Fang et al., CVM-H) show remarkably similar synthetic waveforms. This may be due to the inclusion of longer period data and the relatively shallow depth (~25 km) of the Fang et al. (2016)/Guo models, or could be due to the station geometry (Figure 4), and further analysis is required. For the event shown we cannot determine whether the Guo model has improved waveform fit because of the similarity of the synthetic waveforms from the embedded Guo and Fang et al. (2016) models.

Further work will incorporate more events from diverse locations and will focus on a broad distribution of stations. Emphasis on ray paths traveling through areas where the Fang et al. and Guo models differ will highlight the influence of the updated velocities on waveform fit. In addition, other models will be used to test the sensitivity of waveforms to the embedding procedure. For example, is additional smoothing warranted to ensure sharp boundaries are not artificially introduced? Modeling will also incorporate attenuation as several stations, not shown, exhibited observed data with dominant frequencies lower than those of synthetic waveforms, despite the same filtering procedure. Finally, a re-calibrated density model will be incorporated. The current density model does not incorporate changes in density associated with the varying velocities from the Fang et al./Guo models and hence mirrors the density of the CVM-H model.

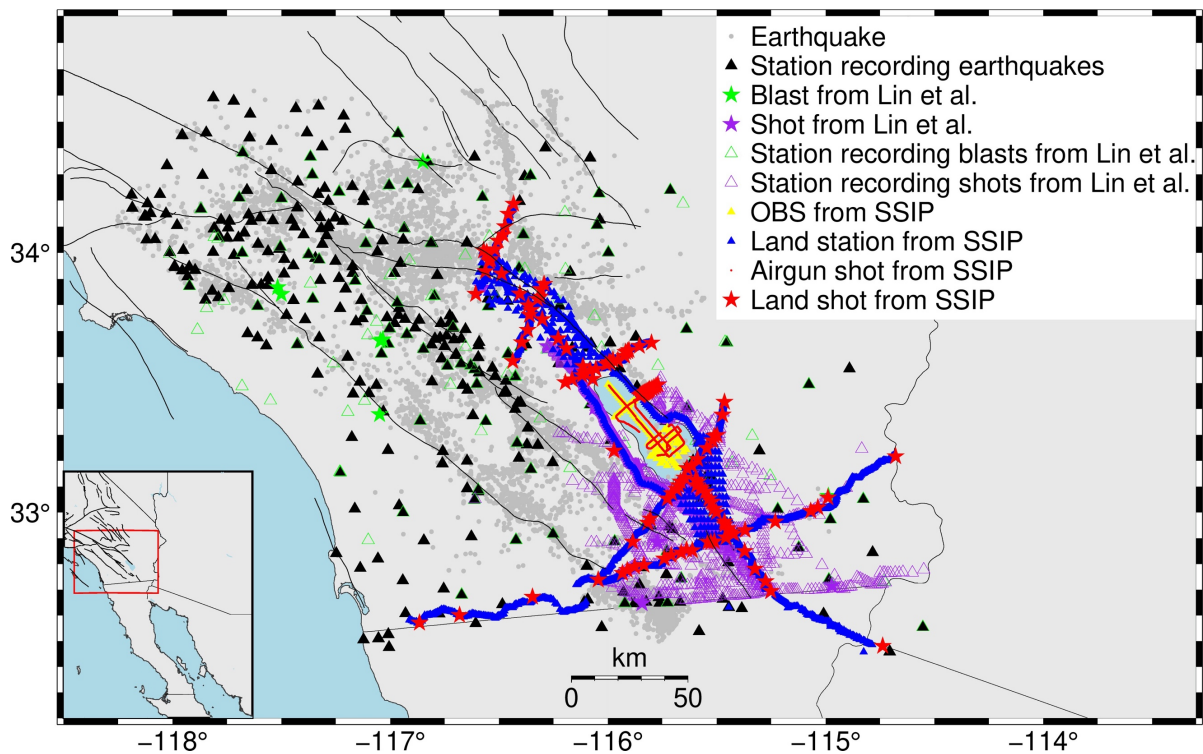


Figure 1. Map of earthquakes, shots, quarry blasts, airgun shots, and network and temporary stations included in our joint inversion analysis.

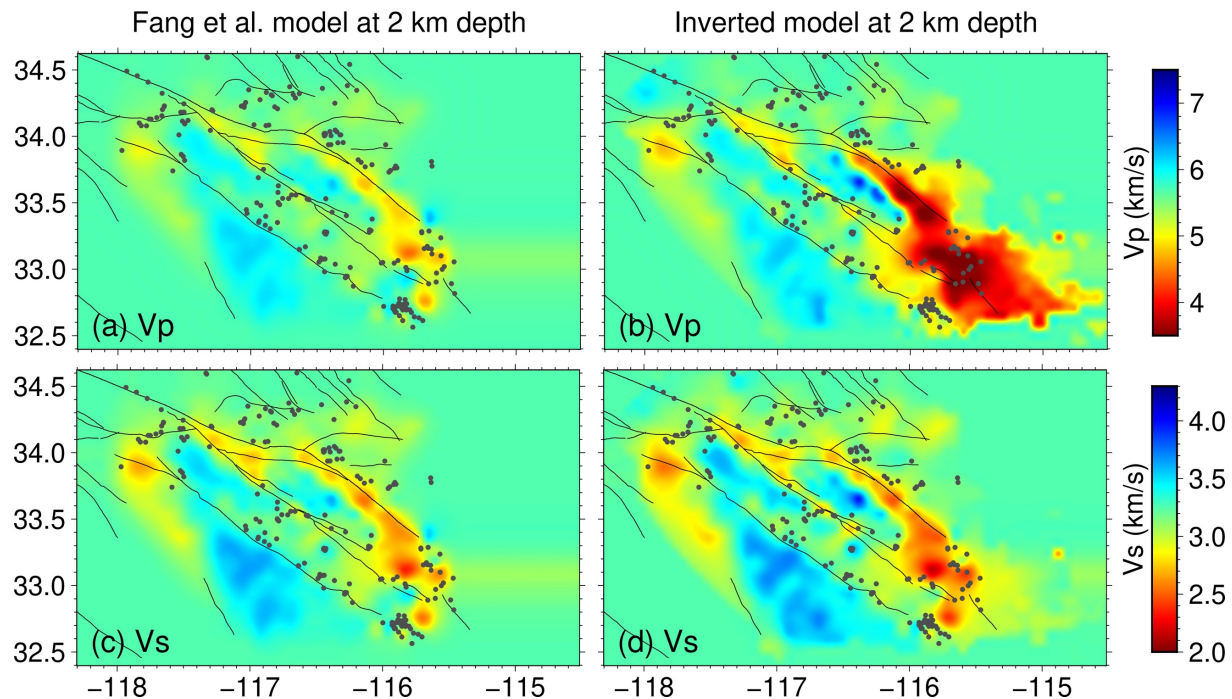


Figure 2. Map-view slices through (left) the Fang et al. (2016) starting model compared to (right) the joint inversion result. (a-b) V_p . (c-d) V_s .

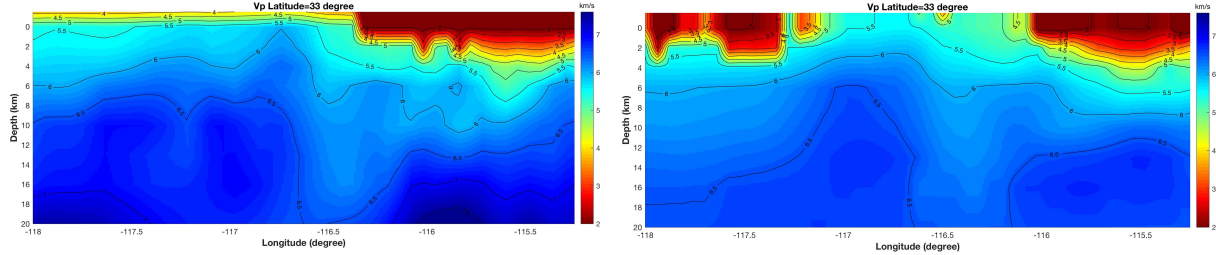


Figure 3. Example CVM-S and CVM-H cross-sections at 33° N, illustrating the extreme horizontal velocity changes at shallow depths that impede the convergence of the spherical-Earth pseudo-bending ray tracer.

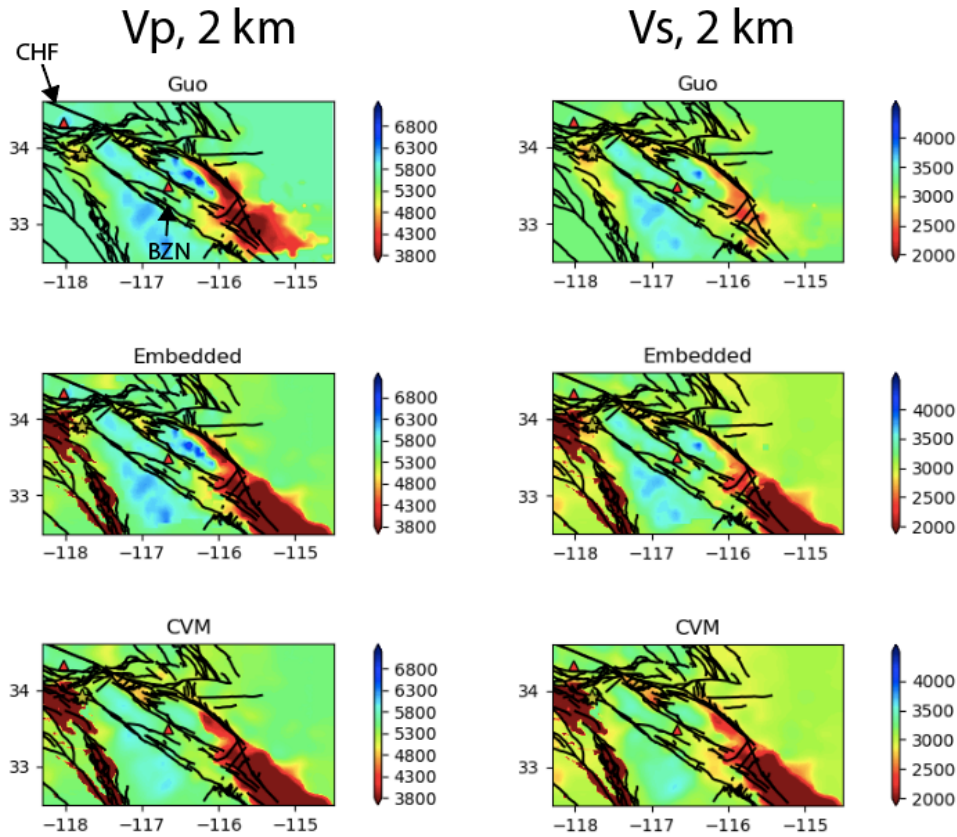


Figure 4. Comparison between the Guo model (prior to embedding, top), the Guo embedded model (middle) and the CVM-H model (bottom) for Vp (left column) and Vs (right column). The embedded model combines the well resolved portions of the Guo model with the broader 3D velocity coverage of the CVM-H model (see higher velocities at -116.5° in both Guo and embedded models and lowered velocities at -117.5° in both embedded and CVM-H model.). Velocity units are m/s. Stations CHF and BZN (labeled top left) are plotted as red triangles. The event epicenter is plotted with a gold star.

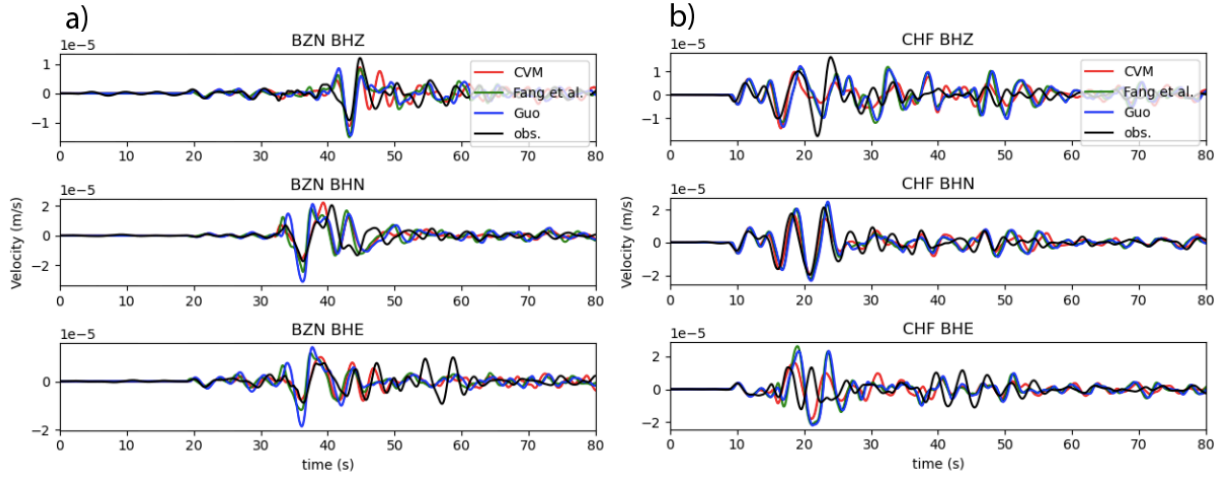


Figure 5. a) Plot of station BZN for components BHZ, BHN, and BHE. The synthetics for CVM-H, for the Fang et al. model and for the Guo model are plotted in red, green and blue respectively. Observations are plotted in black. Data were filtered from 3 to 20 s. b) Same as plot (a) except for station CHF. Synthetics for both BZN and CHF fit the observations reasonably well. Curiously, at this period of interest, there does not appear to be substantial difference between the 3 synthetic models. Locations of stations BZN and CHF relative to the event epicenter are shown in Figure 4.

References

- Fang, H., H. Zhang, H. Yao, A. Allam, D. Zogone, Y. Ben-Zion, C. Thurber, and R. D. van der Hilst (2016), A new algorithm for three-dimensional joint inversion of body-wave and surface-wave data and its application to the Southern California Plate Boundary Region, *J. Geophys. Res. Solid Earth*, 121, doi:10.1002/2015JB012702.
- Guo, H. and Thurber, C. (2021). Double-difference seismic attenuation tomography method and its application to The Geysers geothermal field, California. *Geophys. J. Int.*, 225, 926-949.
- Han, L., et al. (2016), Continental rupture and the creation of new crust in the Salton Trough rift, Southern California and northern Mexico: Results from the Salton Seismic Imaging Project, *J. Geophys. Res. Solid Earth*, 121, 7469-7489, doi:10.1002/2016JB013139.
- Koketsu, K., and S. Sekine, (1998), Pseudo-bending method for three-dimensional seismic ray tracing in a spherical earth with discontinuities, *Geophys. J. Int.*, 132, 339-346.
- Komatitsch, D., Q. Liu, J. Tromp, P. Süss, C. Stidham, and J. H. Shaw (2004), Simulations of ground motion in the Los Angeles basin based upon the spectral-element method, *Bull. Seismol. Soc. Am.*, 94, 187-206, doi:10.1785/0120030077.
- Kristeková, M., J. Kristek, P. Moczo, and S. M. Day (2006), Misfit criteria for quantitative comparison of seismograms, *Bull. Seism. Soc. Am.*, 96, 1836-1850.
- Lin, G., C. H. Thurber, H. Zhang, E. Hauksson, P. M. Shearer, F. Waldhauser, T. M. Brocher, and J. Hardebeck (2010), A California statewide three-dimensional seismic velocity model from both absolute and differential times, *Bull. Seism. Soc. Am.*, 100, 225-240.
- Share, P.-E., H. Guo, C. H. Thurber, H. Zhang, and Y. Ben-Zion (2019), Seismic imaging of the Southern California plate boundary around the South-Central Transverse Ranges using double-difference tomography, *Pure Appl. Geophys.*, 176, 1117-1143, doi: 10.1007/s00024-018-2042-3.
- Um, J., and C. H. Thurber (1987), A fast algorithm for two-point seismic ray tracing, *Bull. Seism. Soc. Am.*, 77, 972-986.
- Waldhauser, F. (2001), HypoDD: A computer program to compute double- difference hypocenter locations, U.S. Geol. Surv. Open File Rep., 01-113, 25 pp.
- Zhang, H., C. Thurber, D. Shelly, S. Ide, G. Beroza, and A. Hasegawa (2004), High-resolution subducting slab structure beneath Northern Honshu, Japan, revealed by double-difference tomography, *Geology*, 32, 361-364.
- Zigone, D., Y. Ben-Zion, M. Campillo, and P. Roux (2015), Seismic tomography of the southern California plate boundary region from noise-based Rayleigh and Love waves, *Pure Appl. Geophys.*, 172, 1007-1032.